

Generative Gaussian Splatting for Unbounded 3D City Generation

Haozhe Xie, Zhaoxi Chen, Fangzhou Hong, Ziwei Liu ✉

S-Lab, Nanyang Technological University

{haozhe.xie, zhaoxi001, fangzhou.hong, ziwei.liu}@ntu.edu.sg

<https://haozhxie.com/project/gaussian-city>

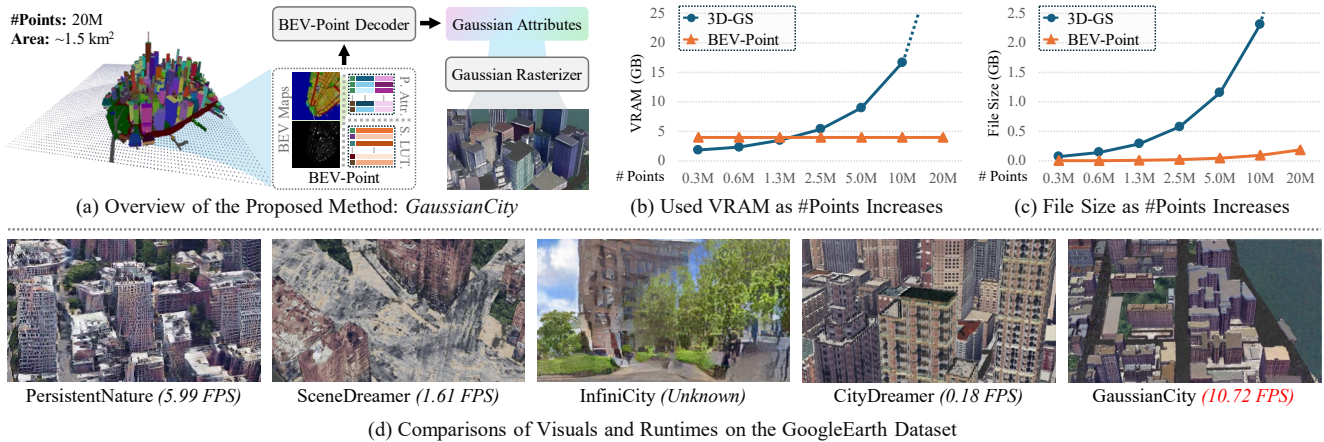


Figure 1. (a) Benefiting from the compact BEV-Point representation, *GaussianCity* can generate unbounded 3D cities using 3D Gaussian splatting (3D-GS). (b) As the number of points increases, VRAM usage during 3D-GS training rises significantly, whereas BEV-Point, acting as a compact representation, maintains a constant VRAM usage. (c) As the number of points increases, BEV-Point exhibits significantly lower growth in file storage compared to 3D-GS. (d) The proposed *GaussianCity* achieves not only superior generation quality but also the best efficiency in 3D city generation.

Abstract

3D city generation with NeRF-based methods shows promising generation results but is computationally inefficient. Recently 3D Gaussian splatting (3D-GS) has emerged as a highly efficient alternative for object-level 3D generation. However, adapting 3D-GS from finite-scale 3D objects and humans to infinite-scale 3D cities is non-trivial. Unbounded 3D city generation entails significant storage overhead (out-of-memory issues), arising from the need to expand points to billions, often demanding hundreds of Gigabytes of VRAM for a city scene spanning 10km². In this paper, we propose **GaussianCity**, a generative Gaussian splatting framework dedicated to efficiently synthesizing unbounded 3D cities with a single feed-forward pass. Our key insights are two-fold: **1) Compact 3D Scene Representation:** We introduce BEV-Point as a highly compact intermediate representation, ensuring that the growth in VRAM usage for unbounded scenes remains constant, thus enabling unbounded city generation. **2) Spatial-aware Gaus-**

sian Attribute Decoder: We present spatial-aware BEV-Point decoder to produce 3D Gaussian attributes, which leverages Point Serializer to integrate the structural and contextual characteristics of BEV points. Extensive experiments demonstrate that *GaussianCity* achieves state-of-the-art results in both drone-view and street-view 3D city generation. Notably, compared to *CityDreamer*, *GaussianCity* exhibits superior performance with a speedup of 60 times (10.72 FPS v.s. 0.18 FPS).

1. Introduction

The generation of 3D assets has attracted considerable attention from both academia and industry due to its significant potential applications. With the rapid advancements in generative modeling, there have been notable achievements in 3D content generation, encompassing the production of objects [12, 51, 53], avatars [10, 19, 23], and scenes [35, 54, 55]. City generation, recognized as one of the most demanding tasks in 3D content creation, holds

wide-ranging applications across domains such as gaming, animation, film, and virtual reality.

In recent years, significant progress has been made in the field of 3D city generation. Both InfiniCity [30] and City-Dreamer [54] employ NeRF [37] to generate unbounded photorealistic 3D cities, achieving promising results. However, these methods sample points at the same density and aggregate color values for all points along rays, resulting in inefficiencies during inference and loss of details. Over the past year, 3D Gaussian splatting (3D-GS) [22] has gained widespread use in 3D generation, offering a significantly faster rendering technique by leveraging GPU-based rasterization. Moreover, 3D-GS provides a more flexible way to represent details, leveraging more 3D Gaussians to capture finer intricacies. However, existing 3D-GS-based generators [13, 33, 51] only produce finite-scale objects or scenes containing a limited number of 3D Gaussians. As illustrated in Figure 1(b-c), when the scene scales up, the demands for GPU memory (VRAM) and file storage grow dramatically, making it infeasible for unbounded scene generation.

To address these issues, we propose **GaussianCity**, the first generative Gaussian splatting for unbounded 3D city generation. As shown in Figure 1(a), GaussianCity leverages a highly compact scene representation, namely BEV-Point, to decouple Gaussian attributes into two major parts: position-related attributes and style-related attributes. The position-related attributes can be further condensed into bird’s-eye-view (BEV) maps, while the style-related attributes can be compressed into a style lookup table. Only visible BEV points are considered during the rendering and optimization process, ensuring that VRAM usage is kept at a constant level. To generate 3D Gaussian attributes from BEV points, we present BEV-Point Decoder, which leverages Point Serializer to capture structural and contextual characteristics of unstructured BEV points. Notably, the contextual characteristics of points are inherently preserved during point sampling within a local 3D patch in NeRF, whereas these are disrupted due to the unstructured nature of BEV points. The Gaussian Rasterizer is finally employed to render the image from the generated Gaussian attributes.

The contributions are summarized as follows:

- To the best of our knowledge, we propose the first 3D-GS generative model for unbounded 3D city generation with both high realism and efficiency.
- We introduce BEV-Point as a highly compact representation, which ensures that the VRAM usage remains constant as the scene size scales up.
- We present BEV-Point Decoder, which leverages Point Serializer to capture both structural and contextual characteristics of unstructured BEV points.
- Extensive experiments showcase the superiority of GaussianCity over state-of-the-art methods for 3D city generation in terms of both generation quality and efficiency.

2. Related Work

3D Gaussian Splatting. 3D Gaussian splatting (3D GS) [22] has gained considerable attention in recent months, demonstrating promising rendering results and faster performance compared to NeRF [37]. Numerous methods have been proposed to integrate 3D GS into the 3D reconstruction of objects [49, 56, 62], avatars [42, 46, 61], and scenes [31, 34, 36]. Furthermore, several approaches [24, 38] have aimed to optimize the high memory consumption of 3D GS during reconstruction. 3D GS is also extensively used in the generation of 3D objects [50, 51], 3D avatars [1, 33, 60], and 3D scenes [13]. However, these methods only generate small-scale 3D assets and are not memory-efficient for representing large-scale 3D assets. Benefiting from 3D-GS, efficiently applying it to 4D object [15, 44] and human [25, 27, 57] generation with deformation becomes feasible.

Scene Generation. Unlike impressive models for generating objects and avatars, generating scenes presents greater challenges due to their extremely high diversity. Earlier approaches [26, 32] generate scenes by synthesizing videos, which lack 3D awareness and cannot ensure 3D consistency. Semantic image synthesis methods [16, 40, 48] exhibit promising results in generating scene-level content by conditioning on pixel-wise dense correspondence, such as semantic segmentation maps or depth maps. Several methods [7, 13, 59] generate natural 3D scenes by performing inpainting and outpainting on RGB images or feature maps. However, most methods can only interpolate or extrapolate a limited distance from the input views and lack generative capabilities. Recent approaches [4, 11, 30, 54] have achieved 3D consistent scenes at an infinite scale through unbounded layout extrapolation. Another set of works focuses on indoor scene synthesis using costly 3D datasets [3, 14] or CAD object retrieval [41].

3. Our Approach

3.1. Background: 3D Gaussian Splatting

As introduced in [22], 3D Gaussian splatting (3D-GS) is an explicit point-based 3D scene representation, using a set of 3D Gaussians with various attributes to model the scene. Each Gaussian is characterized by a center $\mathbf{x} \in \mathbb{R}^3$, a scaling factor of $\mathbf{s} \in \mathbb{R}^3$, and a rotation quaternion $\mathbf{q} \in \mathbb{R}^4$. Additionally, it maintains opacity value $\alpha \in \mathbb{R}$ and a color feature $\mathbf{c} \in \mathbb{R}^C$ for rendering, where spherical harmonics can model view-dependent effects. These parameters can collectively be denoted by $\mathbf{A} = \{\mathbf{x}_i, \mathbf{s}_i, \mathbf{q}_i, \alpha_i, \mathbf{c}_i\}_{i=1}^N$, where N is the number of 3D Gaussians. Rendering 3D Gaussians involves projecting them onto the image plane as 2D Gaussians and performing alpha composition for each pixel in front-to-back depth order, thus determining the final color and alpha.

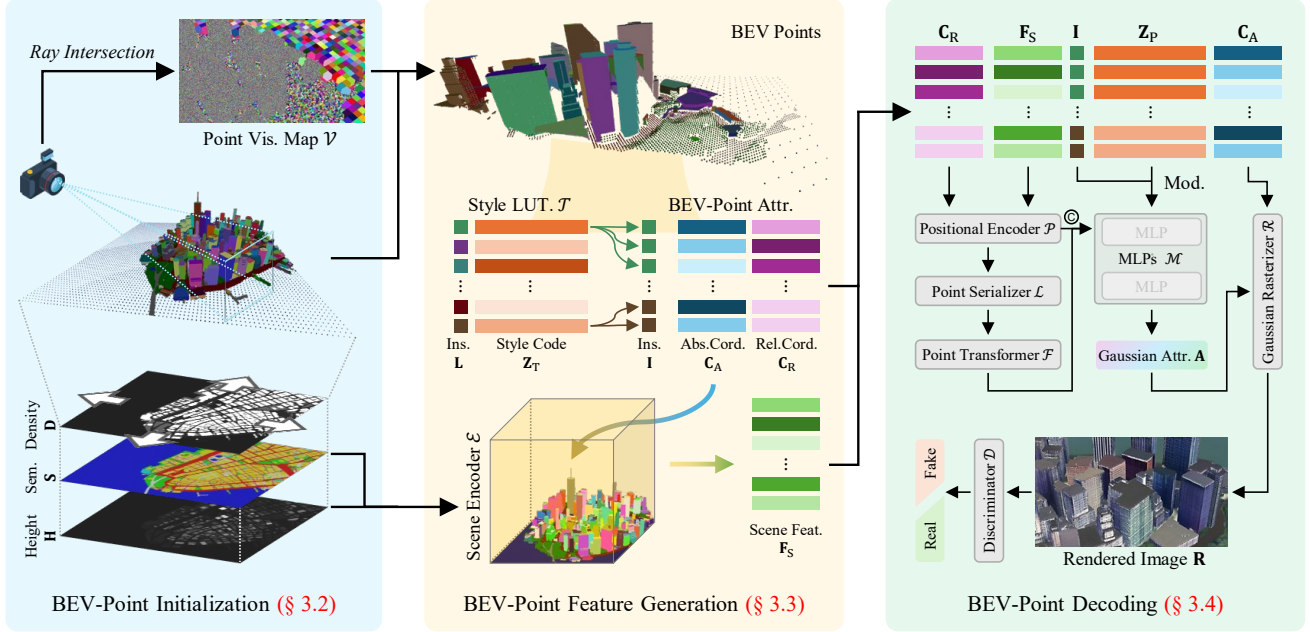


Figure 2. **The framework of GaussianCity.** To create an unbounded 3D city, the BEV points are firstly generated from a local patch of the BEV maps, which includes the height field \mathbf{H} , semantic map \mathbf{S} , and binary density map \mathbf{D} . Then, the BEV-Point attributes $\{\mathbf{I}, \mathbf{C}_A, \mathbf{C}_R, \mathbf{F}_S\}$ are generated for each point and the Style Lookup Table: $\mathcal{T}(\mathbf{L}) \rightarrow \mathbf{Z}_T$ is generated for each instance. Next, BEV-Point Decoder generates the Gaussian attributes \mathbf{A} from BEV-Point attributes. Finally, Gaussian Rasterizer \mathcal{R} produces the rendered image \mathbf{R} .

3.2. BEV-Point Initialization

Within 3D-GS, all 3D Gaussians undergo initialization with a predefined set of parameters during optimization. However, as the scene scales up, the VRAM usage increases dramatically, making it impractical to generate large-scale scenes. Addressing this issue, we propose a highly compact representation namely BEV-Point. In the BEV-Point representation, only visible BEV points are retained since only they impact the appearance of the current frame. It ensures that VRAM usage remains constant because the number of visible BEV points does not increase with the scene scale, given fixed camera parameters.

In a local patch of a bird’s-eye-view (BEV) map comprising a semantic map \mathbf{S} and a height field \mathbf{H} , a collection of BEV points within this patch can be produced by extruding the pixels in the semantic map \mathbf{S} according to the corresponding values in the height field \mathbf{H} . We further introduce the binary density map \mathbf{D} to adjust the sampling density for different semantic categories. This is driven by the observation that certain categories exhibit simpler textures (*e.g.*, roads, water areas), allowing for reduced density to manage computational costs, while other categories (*e.g.*, building façades) possess intricate textures, necessitating a greater number of points for representation. The coordinates of the generated BEV points, denoted as $\mathbf{C}_F \in \mathbb{R}^{N_{pt} \times 3}$, can be generated as

$$\mathbf{C}_F = \{(x, y, z) \mid \mathbf{H}_{(x,y)} \leq z \text{ and } \mathbf{D}_{(x,y)} = 1\} \quad (1)$$

where N_{pt} is the number of BEV points.

Benefiting from the binary density map \mathbf{D} , a significant number of redundant BEV points have been omitted. However, the remaining number, typically 20 million BEV points, is still too large for optimization. To address this issue, we additionally conduct ray intersection to obtain the binary visibility map $\mathcal{V} : (x, y, z) \rightarrow v$, where $v \in \{0, 1\}$, for filtering out the visible BEV points. Therefore, the coordinates of the visible BEV points $\mathbf{C}_A \in \mathbb{R}^{N_{pt} \times 3}$ can be generated as

$$\mathbf{C}_A = \{(x, y, z) \mid (x, y, z) \in \mathbf{C}_F \text{ and } \mathcal{V}(x, y, z) = 1\} \quad (2)$$

3.3. BEV-Point Feature Generation

The features in the BEV-Point representation can be divided into three categories: instance attributes, BEV-Point attributes, and style look-up table. The instance attributes encompass fundamental details such as Instance label, size, and center coordinates for each instance. The BEV-Point attributes determine the appearance within the instance, while the style look-up table controls the style variation across instances.

Instance Attributes. The semantic map \mathbf{S} provides semantic labels for BEV points. Following CityDreamer [54], the instance map \mathbf{Q} is introduced to handle the diversity of buildings and cars in urban environments. Specifically,

$$\mathbf{Q} = \text{Inst}(\mathbf{S}) \quad (3)$$

where $\text{Inst}(\cdot)$ denotes instantiation on semantic maps by detecting connected components. Therefore, the instance label $\mathbf{I} \in \mathbb{R}^{N_{\text{pt}} \times 1}$ for BEV points can be computed as

$$\mathbf{I} = \{\mathbf{Q}_{(x,y)} \mid (x, y, z) \in \mathbf{C}_A\} \quad (4)$$

Obviously, $\mathbf{Q}_{(x,y)} \in \mathbf{L}$, where $\mathbf{L} = \{1, 2, \dots, N_{\text{ins}}\}$ and N_{ins} is the number of instances. The size $\mathcal{S}(l) \in \mathbb{R}^3$ represents the size of the 3D bounding box of the instance l , where $l \in \mathbf{L}$. The center $\mathcal{C}(l) \in \mathbb{R}^3$ denotes the coordinates of the center of the bounding box of the instance l .

BEV-Point Attributes. In BEV-Point initialization, the absolute coordinate \mathbf{C}_A is generated, with the origin set at the center of the world coordinate system. Besides the absolute coordinate, the relative coordinate $\mathbf{C}_R \in \mathbb{R}^{N_{\text{pt}} \times 3}$ is introduced, with its origin set at the center of each instance, to specify the normalized point coordinates relative to the instance. Specifically,

$$\mathbf{C}_R = \{\mathbf{C}_R^i \mid \mathbf{C}_R^i \in \mathbb{R}^3\}_{i=1}^{N_{\text{pt}}} \quad (5)$$

where \mathbf{C}_R^i can be derived as

$$\mathbf{C}_R^i = \frac{2(\mathbf{C}_A^i - \mathcal{C}(\mathbf{I}^i))}{\mathcal{S}(\mathbf{I}^i)} \quad (6)$$

where \mathbf{C}_A^i and \mathbf{I}^i denote the i -th values in \mathbf{C}_A and \mathbf{I} , respectively.

During generation, integrating contextual information for BEV points becomes essential. It is achieved by introducing scene features $\mathbf{F}_S \in \mathbb{R}^{N_{\text{pt}} \times C_{F_S}}$ derived from BEV maps and indexed using absolute coordinates \mathbf{C}_A . Specifically,

$$\mathbf{G} = \mathcal{E}(\mathbf{H}, \mathbf{S}) \quad (7)$$

$$\mathbf{F}_S = \{\mathbf{G}_{(x,y)} \mid (x, y, z) \in \mathbf{C}_A\} \quad (8)$$

where \mathcal{E} denotes the Scene Encoder. \mathbf{G} is with the same size of \mathbf{H} and \mathbf{S} .

Style Look-up Table. In 3D-GS, the appearance of 3D Gaussians is defined by the attributes of each Gaussian. As the number of 3D Gaussians increases, the demands on VRAM and file storage grow significantly, making unbounded scene generation infeasible. To further reduce computational costs, the appearances of instances are encoded into a set of latent vectors $\mathbf{Z}_T \in \mathbb{R}^{N_{\text{ins}} \times C_Z}$, i.e.,

$$\mathbf{Z}_T = \{\mathbf{z}_T^i \mid \mathbf{z}_T^i \in \mathbb{R}^{C_Z}\}_{i=1}^{N_{\text{ins}}} \quad (9)$$

The style look-up table \mathcal{T} queries the style code $\mathbf{z}_T^i \sim \mathcal{N}(0, 1)$ for the instance l . Specifically,

$$\mathbf{z}_T^i = \mathcal{T}(l) \quad (10)$$

3.4. BEV-Point Decoding

The BEV-Point decoder is designed to generate the Gaussian Attributes \mathbf{A} using the BEV-Point features. It comprises five key modules: positional encoder, point serializer, point transformer, modulated MLP, and Gaussian rasterizer.

Positional Encoder. Rather than feed coordinates directly into the subsequent networks, the positional encoder transforms each point coordinate and corresponding features into a higher-dimensional positional embedding $\mathbf{F}_P \in \mathbb{R}^{N_{\text{pt}} \times C_{F_P}}$ as follows

$$\mathbf{F}_P = \mathcal{P}(\text{Concat}(\mathbf{C}_R, \mathbf{F}_S)) \quad (11)$$

where $\mathcal{P}(\cdot)$ is the positional encoding function that is applied individually to each value in the given feature x .

$$\mathcal{P}(x) = \{\sin(2^i \pi x), \cos(2^i \pi x)\}_{i=0}^{N_{\text{PE}}-1} \quad (12)$$

Point Serializer. Unlike NeRF [37], which maintains spatial correlation among sampled points along rays, BEV points and 3D Gaussians are unstructured and unordered due to their irregular nature of point clouds. Therefore, directly applying Multi-layer Perceptrons (MLPs) to generate Gaussian attributes from \mathbf{F}_P may not yield optimal results, as MLPs do not fully consider the structural and contextual characteristics of point clouds.

To transform unstructured BEV points into a structured format, we present the point serializer $\mathcal{L} : (x, y, z) \rightarrow o$, where $o \in \mathbb{Z}$, to convert the point coordinates into an integer reflecting its order within the given BEV points.

$$\mathcal{L}(x, y, z, g) = \left\lfloor \frac{x}{g^2} + \frac{y}{g} + z \right\rfloor \quad (13)$$

where g is the grid size that controls the scale of the discrete space for serialization. This ordering ensures that points are rearranged based on the spatial structure defined by the point serializer, resulting in neighboring points in the data structure being close together in space. Thus, the serialized feature $\mathbf{F}_P^S \in \mathbb{R}^{N_{\text{pt}} \times C_{F_P}}$ can be derived as

$$\mathbf{F}_P^S = \{\mathbf{F}_P^{O_i}\}_{i=1}^{N_{\text{pt}}} \quad (14)$$

where $\mathbf{F}_P^{O_i}$ denotes the features of the O_i -th BEV point in \mathbf{F}_P . O_i denotes the order generated by the point serializer.

Point Transformer. After serialization, the features of BEV points can be processed by a modern Transformer \mathcal{F} [52], producing the feature $\mathbf{F}_T \in \mathbb{R}^{N_{\text{pt}} \times C_{F_T}}$.

$$\mathbf{F}_T = \mathcal{F}(\mathbf{F}_P^S) \quad (15)$$

Modulated MLPs. The attributes of 3D Gaussians $\mathbf{A} \in \mathbb{R}^{N_{\text{pt}} \times C_A}$ are generated by applying MLPs \mathcal{M} [21], which

modulate the style code \mathbf{Z}_P and instance labels \mathbf{I} with the features of BEV points.

$$\mathbf{A} = \mathcal{M}(\text{Concat}(\mathbf{F}_P, \mathbf{F}_T), \mathbf{Z}_P, \mathbf{I}) \quad (16)$$

where $\mathbf{Z}_P = \{\mathcal{T}(\mathbf{I}^i)\}_{i=1}^{N_{pt}}$.

Gaussian Rasterizer. Given the camera intrinsic and extrinsic parameters $\mathbf{K} \in \mathbb{R}^{3 \times 3}$ and $\mathbf{T} \in \mathbb{R}^{4 \times 4}$, the image can be rendered with the Gaussian rasterizer \mathcal{R} .

$$\hat{\mathbf{R}} = \mathcal{R}(\mathbf{C}_A, \mathbf{A}, \mathbf{K}, \mathbf{T}) \quad (17)$$

During rasterization, default values are employed if the required attributes are not generated in \mathbf{A} . These defaults include scale factor $\mathbf{s} = \mathbf{1}$, rotation quaternion $\mathbf{q} = [1, 0, 0, 0]$, and opacity $\alpha = 1$.

3.5. Loss Functions

The generator is trained using a hybrid objective that combines reconstruction loss with adversarial learning loss. Specifically, we leverage the L1 loss, VGG loss [20], and GAN loss [29] in this combination.

$$\ell = \lambda_{L1} \|\hat{\mathbf{R}} - \mathbf{R}\| + \lambda_{VGG} \text{VGG}(\hat{\mathbf{R}}, \mathbf{R}) + \lambda_{GAN} \text{GAN}(\hat{\mathbf{R}}, \mathbf{S}_G) \quad (18)$$

where \mathbf{R} denotes the ground truth image. \mathbf{S}_G is the semantic map in perspective view.

4. Experiments

4.1. Datasets

GoogleEarth [54]. The GoogleEarth dataset, sourced from Google Earth Studio, comprises 400 orbit trajectories captured over Manhattan and Brooklyn. Each trajectory comprises 60 images, with orbit radiuses spanning from 125 to 813 meters and altitudes ranging from 112 to 884 meters. In addition to the images, GoogleEarth provides camera intrinsic and extrinsic parameters, along with 3D semantic and building instance segmentation.

KITTI-360 [28]. KITTI-360 is an extensive outdoor sub-urban dataset known for its intricate scene geometry. Within this dataset, scenes are rich in highlights and shadows, resulting in significant variations in the appearance of objects across different scenes. Captured in urban scenarios spanning approximately 73.7km of driving distance, KITTI-360 provides comprehensive 3D bounding box annotations for various classes such as buildings, cars, roads, vegetation, and more.

4.2. Evaluation Protocols

FID and KID. Fréchet Inception Distance (FID) [17] and Kernel Inception Distance (KID) [5] are metrics for the quality of generated images. Following CityDreamer [54], FID and KID are calculated based on 15K generated frames

on the GoogleEarth dataset. As for the KITTI-360 dataset, FID and KID are computed using 5K generated frames, consistent with the settings of UrbanGIRAFFE [58].

Depth Error. We employ depth error (DE) to assess the 3D geometry following EG3D [8]. The pseudo ground truth depth maps for the generated frames are obtained from a pretrained model [43]. For NeRF-based methods, the depth maps are generated by the accumulation of density σ . Conversely, GaussianCity allows for the direct acquisition of depth maps by rasterization. DE is calculated as the L2 distance between the two normalized depth maps. We evaluate DE using 100 frames for each assessed method following CityDreamer [54].

Camera Error. Following CityDreamer [54], the camera error (CE) is introduced to evaluate the multi-view consistency. CE quantifies the disparity between the inference camera trajectory and the estimated camera trajectory from COLMAP [45], computed as the scale-invariant normalized L2 distance between the reconstructed and generated camera poses.

Runtime. Runtime is used to gauge efficiency. It measures the time taken to generate a 960x540 image on the GoogleEarth dataset. All timings are conducted on an NVIDIA Tesla A100, excluding IO time, and averaged over 100 iterations.

4.3. Implementation Details

Hyperparameters. The grid size g is set to 0.01 and N_{PE} is set to 64. The feature channels C_Z, C_{F_S}, C_{F_P} , and C_{F_T} are set to 256, 61, 1280, and 256, respectively. The Gaussian attributes \mathbf{A} consist of RGB values only (*i.e.*, $C_A = 3$). Initially, the loss weights λ_{L1} , λ_{VGG} , and λ_{GAN} are set to 10, 10, and 0.5, respectively. Afterward, λ_{L1} and λ_{VGG} are reduced by half every 20,000 epochs.

Training Details. The generator is trained using an Adam optimizer with $\beta = (0, 0.999)$ and a learning rate of 10^{-4} . The discriminator is optimized using an Adam optimizer with $\beta = (0, 0.999)$ and a learning rate of 5×10^{-7} . Training continues for 200,000 iterations with a batch size of 8 on eight NVIDIA Tesla V100 GPUs. The images are randomly cropped to sizes of 448x448 for GoogleEarth and 448x224 for KITTI-360.

4.4. Main Results

Comparison Methods. On the GoogleEarth dataset, we compare the proposed method to SGAM [47], Persistent-Nature [7], SceneDreamer [11], InfiniCity [30], and CityDreamer [54], following the protocol established by CityDreamer. Except for InfiniCity, whose code is not accessible, we retrain the remaining methods using the released code on the GoogleEarth dataset to ensure fair comparisons. On the KITTI-360 dataset, we compare our method to StyleGAN2 [21], GSN [14], GIRAFFE [39], and Urban-

Table 1. **Quantitative comparison on GoogleEarth and KITTI-360.** The best results are highlighted in bold. Note that “RT.” denotes “Runtime”, measured in milliseconds on an NVIDIA Tesla A100.

Method	GoogleEarth					KITTI-360		
	FID ↓	KID ↓	DE ↓	CE ↓	RT. ↓	Method	FID ↓	KID ↓
SGAM [47]	277.64	0.358	0.575	239.291	193	StyleGAN [21]	31.9	0.021
Pers.Nature [7]	123.83	0.109	0.326	86.371	167	GSN [14]	160.0	0.114
SceneDreamer [11]	213.56	0.216	0.152	0.186	620	GIRAFFE [39]	112.1	0.117
CityDreamer [54]	97.38	0.096	0.147	0.060	5580	UrbanGIR. [58]	39.6	0.036
GaussianCity	86.94	0.090	0.136	0.057	93	GaussianCity	29.5	0.017

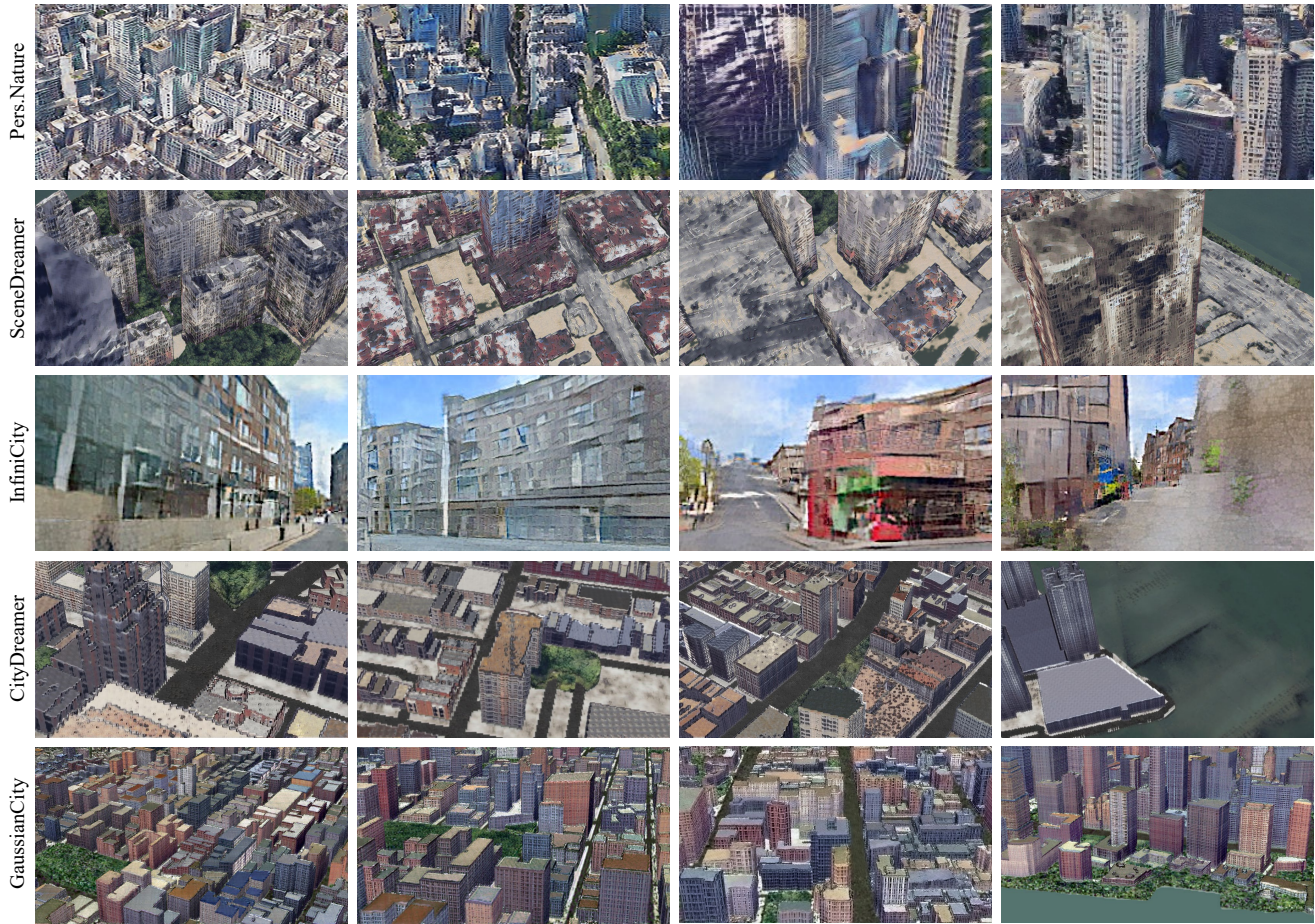


Figure 3. **Qualitative comparison on GoogleEarth.** Note that “Pers.Nature” is short for PersistentNature [7]. The visual results of InfiniCity [30] are provided by the authors since the source code is not accessible.

GIRAFFE [58], following the protocol outlined by UrbanGIRAFFE. As the training code and pretrained model for UrbanGIRAFFE are unavailable, the results of UrbanGIRAFFE are directly obtained from [58].

Comparison on GoogleEarth. Figure 3 shows qualitative comparisons against baselines on the GoogleEarth dataset. PersistentNature utilizes a tri-plane representation, which faces difficulties in generating realistic renderings. Both SceneDreamer and InfiniCity employ voxel grids as their

representation, yet they still encounter significant structural distortions in buildings due to all buildings being assigned the same semantic label. CityDreamer and GaussianCity both introduce instance labels, achieving improved generation results. However, CityDreamer composites two neural fields, resulting in artifacts at the seams of images. In contrast, GaussianCity achieves better visual results and significantly lower runtime, as indicated in Table 1.

Comparison on KITTI-360. Figure 4 illustrates qualita-



Figure 4. **Qualitative comparison on KITTI-360.** The visual results of UrbanGIRAFFE [58] are provided by the authors since the training code and pretrained model are unavailable.

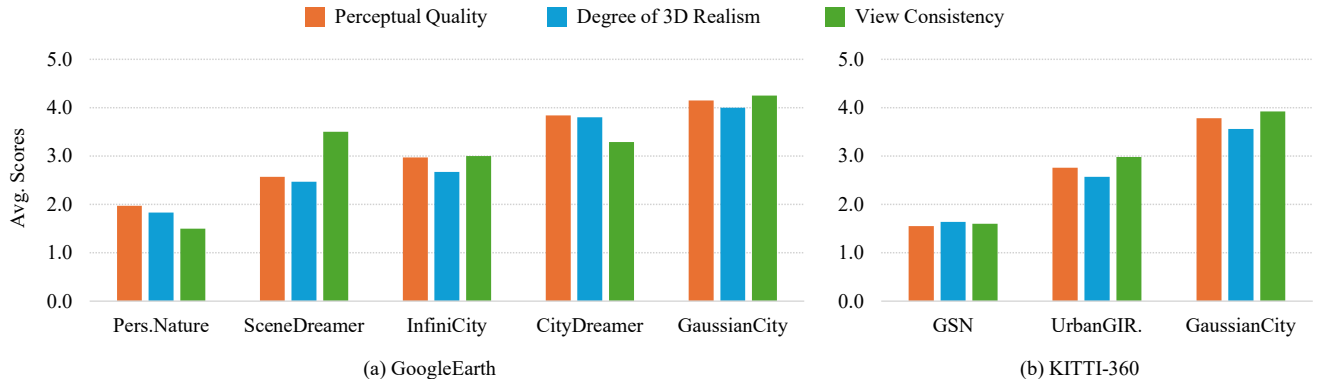


Figure 5. **User study on GoogleEarth and KITTI-360.** All scores are in the range of 5, with 5 indicating the best. Note that “Pers.Nature” and “UrbanGIR.” denotes PersistentNature [7] and UrbanGIRAFFE [58], respectively.

tive comparisons against baseline methods on the KITTI-360 dataset. GSN uses an implicit representation named latent grid, which can easily introduce structural distortion in street-view generation. UrbanGIRAFFE employs a voxel grid as its 3D representation, but due to the resolution limitations of the voxel grid, the generated scenes may exhibit jagged artifacts. In contrast, GaussianCity adopts a more flexible point cloud as its representation, thus yielding superior visual results. The lower FID and KID scores in Table 1 also attest to the effectiveness of the proposed method.

User Study. To more accurately evaluate the 3D consistency and quality of the unbounded 3D city generation, we conduct an output evaluation [6], following the user study conducted in CityDreamer. In this study, we requested feed-

back from 20 volunteers to assess each generated camera trajectory based on three criteria: 1) the perceptual quality of the imagery, 2) the level of 3D realism, and 3) the 3D view consistency. Ratings are provided on a scale of 1 to 5, with 5 indicating the highest rating. The results are shown in Figure 5, demonstrating that the proposed method significantly surpasses the baselines by a considerable margin.

4.5. Ablation Studies

Effectiveness of BEV-Point Representation. The proposed BEV-Points, a compact scene representation, are essential for enabling 3D-GS to generate unbounded scenes by 1) considering point visibility during generation and 2) adjusting sampling density for different semantic cate-

Table 2. **Effectiveness of BEV-Point Representation.** Note that “RayInt.” denotes “Ray Intersection”, respectively. The VRAM usage and inference time are measured on an NVIDIA Tesla A100.

Visibility	Density	#Points	VRAM (G)	Time (s)
\times	\times	31M	Out of Memory	
\times	\checkmark	20M	Out of Memory	
Region	\checkmark	1.4M	Out of Memory	
Instance	\checkmark	680K	10.34	0.16
RayInt.	\times	38.0K	1.41	0.10
RayInt.	\checkmark	31.7K	1.39	0.09

Table 3. **Effectiveness of BEV-Point Decoder.** Note that “Ser.” and “Pt.Trans.” denote “Point Serializer” and “Point Transformer”, respectively.

Ser.	Pt.Trans.	FID \downarrow	KID \downarrow	DE \downarrow	CE \downarrow
\times	\times	151.27	0.179	0.185	0.135
\times	\checkmark	119.40	0.138	0.159	0.118
\checkmark	\checkmark	86.94	0.090	0.136	0.057

Table 4. **Comparison of different serialization methods.** Note that “Eq. 13” denote the serialization used in Point Serializer.

Eq. 13	Hilbert	FID \downarrow	KID \downarrow	DE \downarrow	CE \downarrow
\checkmark	\times	86.94	0.090	0.136	0.057
\times	\checkmark	86.72	0.088	0.136	0.056
\checkmark	\checkmark	86.28	0.083	0.135	0.055

gories using a binary density map. Table 2 compares different methods for considering point visibility, including no consideration, region-based, instance-based, and ray-intersection-based strategies for point selection. All methods keep the number of points constant: “region-based” selects points within the camera coverage, “Instance-based” selects visible instances, and “ray-intersection-based” identifies visible points through ray intersection [2]. The “ray-intersection-based” method is the most efficient compared to “region-based” and “instance-based” approaches, eliminating the most invisible points and reducing the total number of points by 97.7% and 96%, respectively. The density map is crucial in the BEV-Point representation because it reduces the number of points for semantic categories that have less texture and need fewer points. As shown in Table 2, removing the density map increases the point count by 20%-50%. As shown in Figure 1(b-c), the proposed BEV-Point representation maintains constant VRAM usage during training, unlike the original 3D-GS [22], which is impractical for unbounded scene generation due to excessive VRAM consumption. Additionally, it significantly reduces file storage as the number of points increases.

Effectiveness of BEV-Point Decoder. BEV-Point Decoder

consists of two key components: *Point Serializer* and *Point Transformer*. As shown in Table 3 and Figure 6, removing both components leads to a significant degeneration due to the absence of spatial correlations. Introducing only the Point Transformer partially establishes spatial correlation, but it does not achieve the same effectiveness as using both components together.

Effectiveness of Serialization Methods. To investigate the impact of different serialization methods in point serializer, we compare the effects of using Equation 13, Hilbert curve [18] adopted in [9, 52], and both simultaneously on the generation results. As shown in Table 4, different serialization methods have minimal impact on the final generation results. We employ Equation 13 in Point Serializer because of its reduced computational complexity. Kindly refer to Figure 7 for more qualitative comparisons.

4.6. Limitations

While our method demonstrates promising results for unconditional 3D city generation, it still has several limitations. Firstly, the BEV-Point Initialization elevates points to a height based on the corresponding value in the height field, which assumes buildings adhere to the Manhattan assumption and cannot represent hollow structures. Secondly, the BEV-Point decoder does not fully exploit the expressive capacity of 3D-GS, as it only predicts RGB in the Gaussian attributes. However, predicting an excessive number of attributes simultaneously may destabilize the training process. Kindly refer to the discussion in Section A.2.

5. Conclusion

In this paper, we introduce GaussianCity for generating unbounded 3D cities. It is the first method to employ 3D-GS for unbounded scene generation. We introduce BEV-Point, a highly compact scene representation to mitigate the substantial increase in VRAM usage associated with representing large-scale scenes using 3D-GS. Additionally, we present BEV-Point Decoder, which leverages Point Serializer to capture the structural and contextual characteristics of unordered BEV points. Compared to previous methods, GaussianCity achieves better visual results and a 60-fold increase in runtime speed compared to CityDreamer. Extensive experimental results demonstrate the effectiveness of the proposed GaussianCity in generating both drone-view and street-view in city scenes.

Acknowledgements. This study is supported by the Ministry of Education, Singapore, under its MOE AcRF Tier 2 (MOET2EP20221-0012, MOE-T2EP20223-0002), NTU NAP, and under the RIE2020 Industry Alignment Fund – Industry Collaboration Projects (IAF-ICP) Funding Initiative, as well as cash and in-kind contribution from the industry partner(s).

References

- [1] Rameen Abdal, Wang Yifan, Zifan Shi, Yinghao Xu, Ryan Po, Zhengfei Kuang, Qifeng Chen, Dit-Yan Yeung, and Gordon Wetzstein. Gaussian shell maps for efficient 3D human generation. In *CVPR*, 2024. 2
- [2] John Amanatides and Andrew Woo. A fast voxel traversal algorithm for ray tracing. In *Eurographics*, 1987. 8
- [3] Miguel Ángel Bautista, Pengsheng Guo, Samira Abnar, Walter Talbott, Alexander Toshev, Zhuoyuan Chen, Laurent Dinh, Shuangfei Zhai, Hanlin Goh, Daniel Ulbricht, Afshin Dehghan, and Joshua M. Susskind. GAUDI: A neural architect for immersive 3D scene generation. In *NeurIPS*, 2022. 2
- [4] Hengwei Bian, Lingdong Kong, Haozhe Xie, Liang Pan, Yu Qiao, and Ziwei Liu. DynamicCity: Large-scale LiDAR generation from dynamic scenes. In *ICLR*, 2025. 2
- [5] Mikolaj Binkowski, Danica J. Sutherland, Michael Arbel, and Arthur Gretton. Demystifying MMD GANs. In *ICLR*, 2018. 5
- [6] Zoya Bylinskii, Laura Mariah Herman, Aaron Hertzmann, Stefanie Hutka, and Yile Zhang. Towards better user studies in computer graphics and vision. *Foundations and Trends in Computer Graphics and Vision*, 15(3):201–252, 2023. 7
- [7] Lucy Chai, Richard Tucker, Zhengqi Li, Phillip Isola, and Noah Snavely. Persistent Nature: A generative model of unbounded 3D worlds. In *CVPR*, 2023. 2, 5, 6, 7, 14, 15
- [8] Eric R. Chan, Connor Z. Lin, Matthew A. Chan, Koki Nagano, Boxiao Pan, Shalini De Mello, Orazio Gallo, Leonidas J. Guibas, Jonathan Tremblay, Sameh Khamis, Tero Karras, and Gordon Wetzstein. Efficient geometry-aware 3D generative adversarial networks. In *CVPR*, 2022. 5
- [9] Wanli Chen, Xinge Zhu, Guojin Chen, and Bei Yu. Efficient point cloud analysis using hilbert curve. In *ECCV*, 2022. 8
- [10] Zhaoxi Chen, Fangzhou Hong, Haiyi Mei, Guangcong Wang, Lei Yang, and Ziwei Liu. PrimDiffusion: Volumetric primitives diffusion for 3D human generation. In *NeurIPS*, 2023. 1
- [11] Zhaoxi Chen, Guangcong Wang, and Ziwei Liu. SceneDreamer: Unbounded 3D scene generation from 2D image collections. *IEEE TPAMI*, 45(12):15562–15576, 2023. 2, 5, 6
- [12] Zhaoxi Chen, Jiayang Tang, Yuhao Dong, Ziang Cao, Fangzhou Hong, Yushi Lan, Tengfei Wang, Haozhe Xie, Tong Wu, Shunsuke Saito, Liang Pan, Dahua Lin, and Ziwei Liu. 3DTopia-XL: High-quality 3D PBR asset generation via primitive diffusion. In *CVPR*, 2025. 1
- [13] Jaeyoung Chung, Suyoung Lee, Hyeongjin Nam, Jaerin Lee, and Kyoung Mu Lee. LucidDreamer: Domain-free generation of 3D Gaussian splatting scenes. In *CVPR*, 2024. 2
- [14] Terrance DeVries, Miguel Ángel Bautista, Nitish Srivastava, Graham W. Taylor, and Joshua M. Susskind. Unconstrained scene generation with locally conditioned radiance fields. In *ICCV*, 2021. 2, 5, 6
- [15] Quankai Gao, Qiangeng Xu, Zhe Cao, Ben Mildenhall, Wen-chao Ma, Le Chen, Danhang Tang, and Ulrich Neumann. GaussianFlow: Splatting Gaussian dynamics for 4D content creation. *arXiv*, 2403.12365, 2024. 2
- [16] Zekun Hao, Arun Mallya, Serge J. Belongie, and Ming-Yu Liu. GANCraft: unsupervised 3D neural rendering of minecraft worlds. In *ICCV*, 2021. 2
- [17] Martin Heusel, Hubert Ramsauer, Thomas Unterthiner, Bernhard Nessler, and Sepp Hochreiter. GANs trained by a two time-scale update rule converge to a local nash equilibrium. In *NIPS*, 2017. 5
- [18] David Hilbert. Über die stetige abbildung einer linie auf ein flächenstück. *Mathematische Annalen*, 38:459–460, 1891. 8
- [19] Fangzhou Hong, Mingyuan Zhang, Liang Pan, Zhongang Cai, Lei Yang, and Ziwei Liu. AvatarCLIP: zero-shot text-driven generation and animation of 3D avatars. *ACM TOG*, 41(4):161:1–161:19, 2022. 1
- [20] Justin Johnson, Alexandre Alahi, and Li Fei-Fei. Perceptual losses for real-time style transfer and super-resolution. In *ECCV*, 2016. 5
- [21] Tero Karras, Samuli Laine, Miika Aittala, Janne Hellsten, Jaakko Lehtinen, and Timo Aila. Analyzing and improving the image quality of styleGAN. In *CVPR*, 2020. 4, 5, 6
- [22] Bernhard Kerbl, Georgios Kopanas, Thomas Leimkühler, and George Drettakis. 3D Gaussian splatting for real-time radiance field rendering. *ACM TOG*, 42(4):139:1–139:14, 2023. 2, 8, 12
- [23] Nikos Kolotouros, Thiemo Alldieck, Andrei Zanfir, Eduard Gabriel Bazavan, Mihai Fieraru, and Cristian Sminchisescu. DreamHuman: Animatable 3D avatars from text. In *NeurIPS*, 2023. 1
- [24] Joo Chan Lee, Daniel Rho, Xiangyu Sun, Jong Hwan Ko, and Eunbyung Park. Compact 3D Gaussian representation for radiance field. In *CVPR*, 2024. 2
- [25] Jiahui Lei, Yufu Wang, Georgios Pavlakos, Lingjie Liu, and Kostas Daniilidis. GART: Gaussian articulated template models. In *CVPR*, 2024. 2
- [26] Zhengqi Li, Qianqian Wang, Noah Snavely, and Angjoo Kanazawa. InfiniteNature-Zero: Learning perpetual view generation of natural scenes from single images. In *ECCV*, 2022. 2
- [27] Zhe Li, Zerong Zheng, Lizhen Wang, and Yebin Liu. Animatable Gaussians: Learning pose-dependent Gaussian maps for high-fidelity human avatar modeling. In *CVPR*, 2024. 2
- [28] Yiyi Liao, Jun Xie, and Andreas Geiger. KITTI-360: A novel dataset and benchmarks for urban scene understanding in 2D and 3D. *IEEE TPAMI*, 45(3):3292–3310, 2023. 5
- [29] Jae Hyun Lim and Jong Chul Ye. Geometric GAN. *arXiv*, 1705.02894, 2017. 5
- [30] Chieh Hubert Lin, Hsin-Ying Lee, Willi Menapace, Menglei Chai, Aliaksandr Siarohin, Ming-Hsuan Yang, and Sergey Tulyakov. InfiniCity: Infinite-scale city synthesis. In *ICCV*, 2023. 2, 5, 6, 14, 15
- [31] Jiaqi Lin, Zhihao Li, Xiao Tang, Jianzhuang Liu, Shiyong Liu, Jiayue Liu, Yangdi Lu, Xiaofei Wu, Songcen Xu, Youliang Yan, and Wenming Yang. VastGaussian: Vast 3D Gaussians for large scene reconstruction. In *CVPR*, 2024. 2

- [32] Andrew Liu, Ameesh Makadia, Richard Tucker, Noah Snavely, Varun Jampani, and Angjoo Kanazawa. Infinite Nature: Perpetual view generation of natural scenes from a single image. In *ICCV*, 2021. 2
- [33] Xian Liu, Xiaohang Zhan, Jiayang Tang, Ying Shan, Gang Zeng, Dahua Lin, Xihui Liu, and Ziwei Liu. HumanGaussian: Text-driven 3D human generation with Gaussian splatting. In *CVPR*, 2024. 2
- [34] Yang Liu, He Guan, Chuanchen Luo, Lue Fan, Junran Peng, and Zhaoxiang Zhang. CityGaussian: Real-time high-quality large-scale scene rendering with Gaussians. In *ECCV*, 2024. 2
- [35] Fan Lu, Kwan-Yee Lin, Yan Xu, Hongsheng Li, Guang Chen, and Changjun Jiang. Urban Architect: Steerable 3D urban scene generation with layout prior. *arXiv*, 2404.06780, 2024. 1
- [36] Tao Lu, Mulin Yu, Linning Xu, Yuanbo Xiangli, Limin Wang, Dahua Lin, and Bo Dai. Scaffold-GS: Structured 3D Gaussians for view-adaptive rendering. In *CVPR*, 2024. 2
- [37] Ben Mildenhall, Pratul P. Srinivasan, Matthew Tancik, Jonathan T. Barron, Ravi Ramamoorthi, and Ren Ng. NeRF: Representing scenes as neural radiance fields for view synthesis. In *ECCV*, 2020. 2, 4
- [38] Simon Niedermayr, Josef Stumpfegger, and Rüdiger Westermann. Compressed 3D Gaussian splatting for accelerated novel view synthesis. In *CVPR*, 2024. 2
- [39] Michael Niemeyer and Andreas Geiger. GIRAFFE: representing scenes as compositional generative neural feature fields. In *CVPR*, 2021. 5, 6
- [40] Taesung Park, Ming-Yu Liu, Ting-Chun Wang, and Jun-Yan Zhu. Semantic image synthesis with spatially-adaptive normalization. In *CVPR*, 2019. 2
- [41] Despoina Paschalidou, Amlan Kar, Maria Shugrina, Karsten Kreis, Andreas Geiger, and Sanja Fidler. ATISS: autoregressive transformers for indoor scene synthesis. In *NeurIPS*, 2021. 2
- [42] Shenhan Qian, Tobias Kirschstein, Liam Schoneveld, Davide Davoli, Simon Giebenhain, and Matthias Nießner. GaussianAvatars: Photorealistic head avatars with rigged 3D Gaussians. In *CVPR*, 2024. 2
- [43] René Ranftl, Katrin Lasinger, David Hafner, Konrad Schindler, and Vladlen Koltun. Towards robust monocular depth estimation: Mixing datasets for zero-shot cross-dataset transfer. *IEEE TPAMI*, 44(3):1623–1637, 2022. 5
- [44] Jiawei Ren, Liang Pan, Jiayang Tang, Chi Zhang, Ang Cao, Gang Zeng, and Ziwei Liu. DreamGaussian4D: Generative 4D Gaussian splatting. *arXiv*, 2312.17142, 2023. 2
- [45] Johannes L. Schönberger and Jan-Michael Frahm. Structure-from-motion revisited. In *CVPR*, 2016. 5
- [46] Zhijing Shao, Zhaolong Wang, Zhuang Li, Duotun Wang, Xiangru Lin, Yu Zhang, Mingming Fan, and Zeyu Wang. SplattingAvatar: Realistic real-time human avatars with mesh-embedded Gaussian splatting. In *CVPR*, 2024. 2
- [47] Yuan Shen, Wei-Chiu Ma, and Shenlong Wang. SGAM: building a virtual 3D world through simultaneous generation and mapping. In *NeurIPS*, 2022. 5, 6
- [48] Zifan Shi, Yujun Shen, Jiapeng Zhu, Dit-Yan Yeung, and Qifeng Chen. 3D-aware indoor scene synthesis with depth priors. In *ECCV*, 2022. 2
- [49] Stanislaw Szymanowicz, Christian Rupprecht, and Andrea Vedaldi. Splatter image: Ultra-fast single-view 3D reconstruction. In *CVPR*, 2024. 2
- [50] Jiayang Tang, Zhaoxi Chen, Xiaokang Chen, Tengfei Wang, Gang Zeng, and Ziwei Liu. LGM: large multi-view Gaussian model for high-resolution 3D content creation. In *ECCV*, 2024. 2
- [51] Jiayang Tang, Jiawei Ren, Hang Zhou, Ziwei Liu, and Gang Zeng. DreamGaussian: Generative Gaussian splatting for efficient 3D content creation. In *ICLR*, 2024. 1, 2
- [52] Xiaoyang Wu, Li Jiang, Peng-Shuai Wang, Zhijian Liu, Xihui Liu, Yu Qiao, Wanli Ouyang, Tong He, and Hengshuang Zhao. Point transformer V3: simpler, faster, stronger. In *CVPR*, 2024. 4, 8
- [53] Haozhe Xie, Hongxun Yao, Shengping Zhang, Shangchen Zhou, and Wenxiu Sun. Pix2Vox++: Multi-scale context-aware 3D object reconstruction from single and multiple images. *IJCV*, 128(12):2919–2935, 2020. 1
- [54] Haozhe Xie, Zhaoxi Chen, Fangzhou Hong, and Ziwei Liu. CityDreamer: Compositional generative model of unbounded 3D cities. In *CVPR*, 2024. 1, 2, 3, 5, 6
- [55] Haozhe Xie, Zhaoxi Chen, Fangzhou Hong, and Ziwei Liu. CityDreamer4D: Compositional generative model of unbounded 4D cities. *arXiv*, 2501.08983, 2025. 1
- [56] Yinghao Xu, Zifan Shi, Wang Yifan, Hansheng Chen, Ceyuan Yang, Sida Peng, Yujun Shen, and Gordon Wetstein. GRM: Large Gaussian reconstruction model for efficient 3D reconstruction and generation. *arXiv*, 2403.14621, 2024. 2
- [57] Zhen Xu, Sida Peng, Haotong Lin, Guangzhao He, Jiaming Sun, Yujun Shen, Hujun Bao, and Xiaowei Zhou. 4K4D: Real-time 4D view synthesis at 4K resolution. In *CVPR*, 2024. 2
- [58] Yuanbo Yang, Yifei Yang, Hanlei Guo, Rong Xiong, Yue Wang, and Yiyi Liao. UrbanGIRAFFE: Representing urban scenes as compositional generative neural feature fields. In *ICCV*, 2023. 5, 6, 7, 16
- [59] Hong-Xing Yu, Haoyi Duan, Junhwa Hur, Kyle Sargent, Michael Rubinstein, William T. Freeman, Forrester Cole, Deqing Sun, Noah Snavely, Jiajun Wu, and Charles Herrmann. WonderJourney: Going from anywhere to everywhere. In *CVPR*, 2024. 2
- [60] Ye Yuan, Xueting Li, Yangyi Huang, Shalini De Mello, Koki Nagano, Jan Kautz, and Umar Iqbal. Gavatar: Animatable 3D Gaussian avatars with implicit mesh learning. In *CVPR*, 2024. 2
- [61] Shunyuan Zheng, Boyao Zhou, Ruizhi Shao, Boning Liu, Shengping Zhang, Liqiang Nie, and Yebin Liu. Gps-Gaussian: Generalizable pixel-wise 3D Gaussian splatting for real-time human novel view synthesis. In *CVPR*, 2024. 2
- [62] Zi-Xin Zou, Zhipeng Yu, Yuan-Chen Guo, Yangguang Li, Ding Liang, Yan-Pei Cao, and Song-Hai Zhang. Triplane meets Gaussian splatting: Fast and generalizable single-view 3D reconstruction with transformers. In *CVPR*, 2024. 2

A. Additional Ablation Study Results

A.1. Qualitative Results for Ablation Studies

Effectiveness of BEV-Point Decoder. Figure 6 gives a qualitative comparison as a supplement to Table 3, demonstrating the effectiveness of Point Serializer and Point Transformer in BEV-Point Decoder. Removing either of them significantly degrades the quality of the generated images.

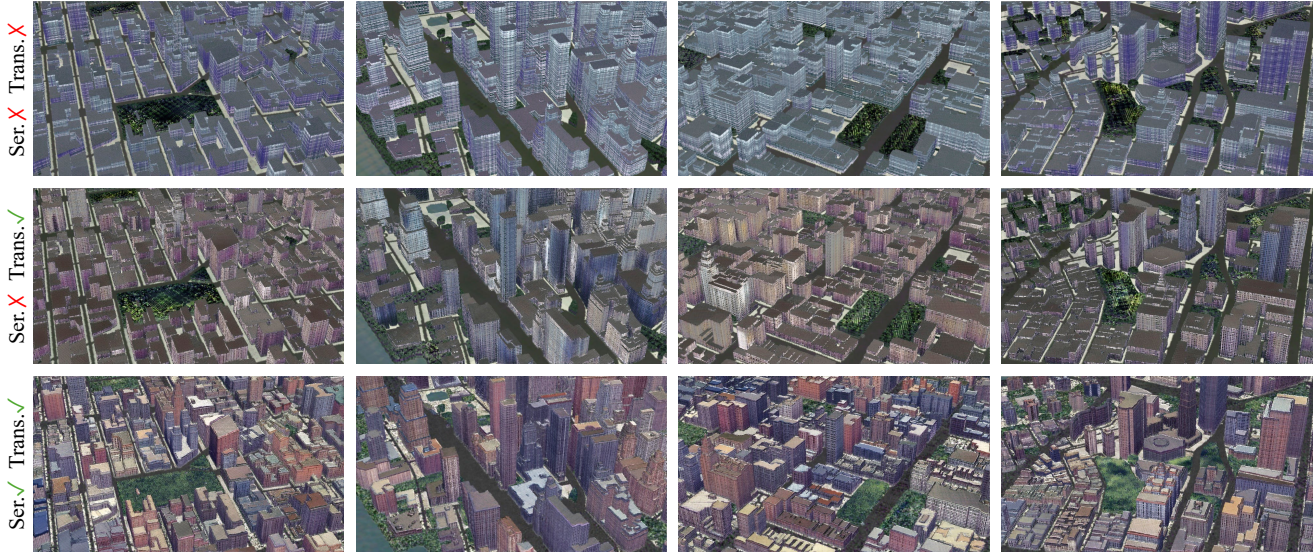


Figure 6. **Qualitative comparison of different BEV-Point Decoder variants.** Note that “Ser.” and “Trans.” represent “Point Serializer” and “Point Transformer”, respectively.

Effectiveness of Different Serialization Methods. Figure 7 provides a qualitative comparison as a supplement to Table 4. As shown in Figure 7, using either Equation 13, the Hilbert curve, or both for serialization is unlikely to impact the quality of the generated results. Moreover, Equation 13 exhibits significantly lower computational complexity compared to the Hilbert curve. Therefore, Equation 13 is employed in the Point Serializer due to its lower computational demands.

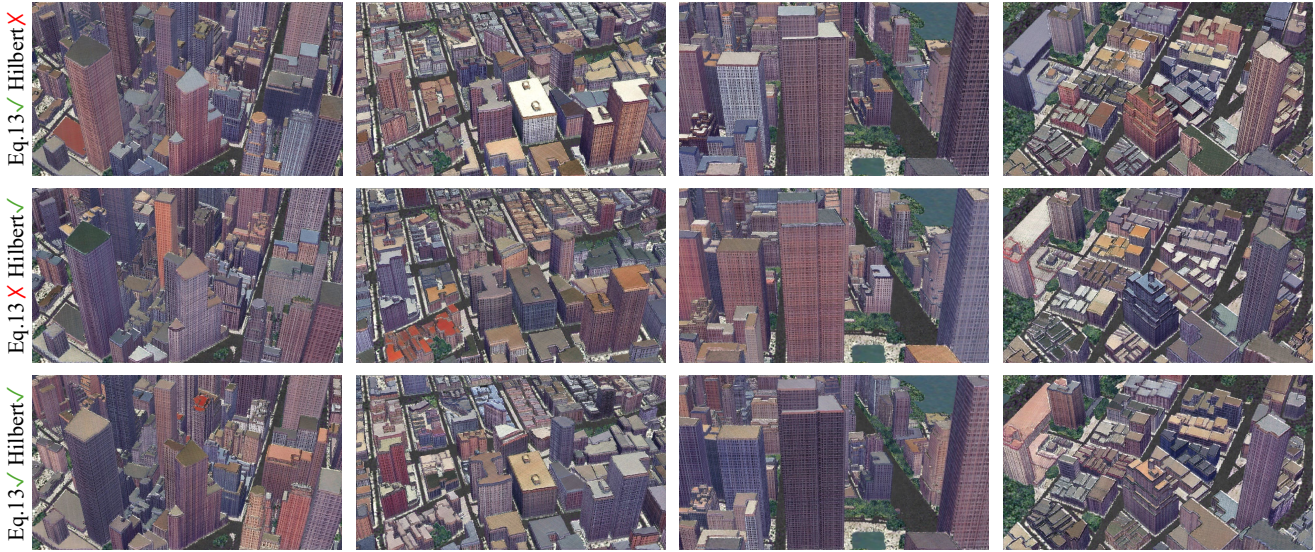


Figure 7. **Qualitative comparison of different serialization methods.** Note that “Eq. 13” denote the serialization used in Point Serializer.

A.2. Discussion on Generated Gaussian Attributes

In 3D-GS [22], each 3D Gaussian possesses multiple attributes, including XYZ coordinates, spherical harmonics (SHs), opacity, rotation, and scale. These attributes are optimized using supervision from multi-view images to represent the scene. In reconstruction, adding extra attributes like XYZ offsets and opacity enhances representation capability. However, a scene can have multiple valid reconstruction results because different combinations of 3D Gaussian attributes can yield the same rendering result. For instance, changing the color of one 3D Gaussian can be equivalent to overlaying multiple Gaussians with varying opacities or adjusting the scale of nearby Gaussians with similar colors. This ambiguity causes instability when optimizing all these attributes simultaneously in city generation.

Due to the carefully designed BEV-Point initialization, all points are evenly distributed on the surface of objects. Therefore, Gaussian attributes other than RGB can be left unestimated and set to their default values. Table 5 and Figure 8 provide a quantitative and qualitative comparison of various attributes generated for 3D Gaussians, demonstrating that optimizing 3D Gaussian attributes beyond RGB not only complicates network convergence but also significantly impacts the quality of the generated results.

Table 5. **Quantitative comparison of different attributes generated for 3D Gaussians.** The best results are highlighted in bold. Note that “-” in CE indicates that COLMAP cannot estimate camera poses from the generated images.

Generated Attributes				GoogleEarth				KITTI-360	
RGB	ΔXYZ	Opacity	Scale	FID ↓	KID ↓	DE ↓	CE ↓	FID ↓	KID ↓
✓	✗	✗	✗	86.94	0.090	0.136	0.057	29.5	0.017
✓	✓	✗	✗	371.15	0.468	0.367	-	281.5	0.342
✓	✓	✓	✗	384.81	0.485	0.401	-	256.9	0.297
✓	✓	✓	✓	535.49	0.709	0.470	-	486.3	0.605

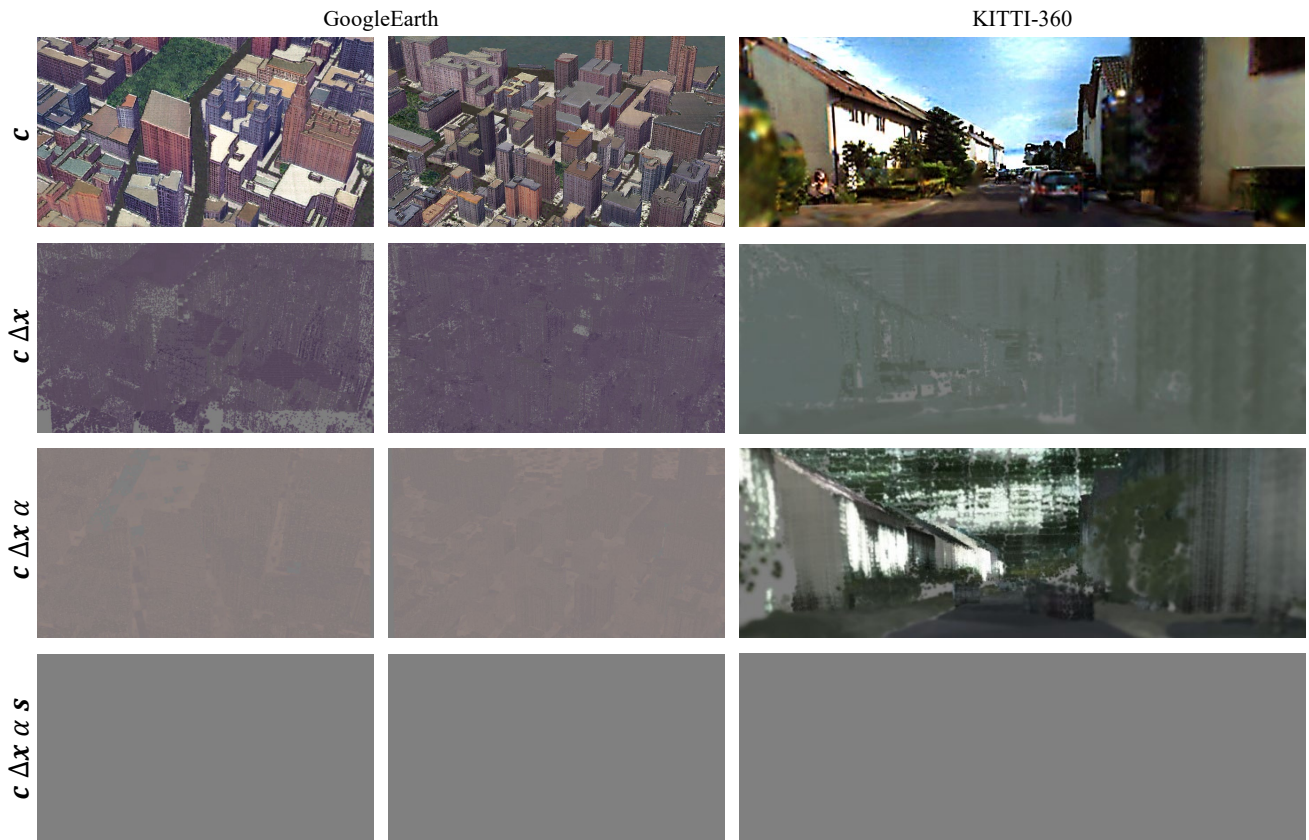


Figure 8. **Qualitative comparison of different attributes generated for 3D Gaussians.** Note that c , Δx , α , and s denote the RGB color, XYZ offsets, opacity, and scale in the generated 3D Gaussian attributes, respectively.

B. Additional Experimental Results

B.1. Building Interpolation

As shown in Figure 9, GaussianCity showcases the capability to interpolate building styles controlled by the variable z . In the first row, local editing is applied by altering only the style code z of the buildings within the bounding boxes, leaving the styles of the other buildings unchanged. In the second row, the style codes of all the buildings are interpolated from left to right, resulting in a gradual style transition across the entire row.

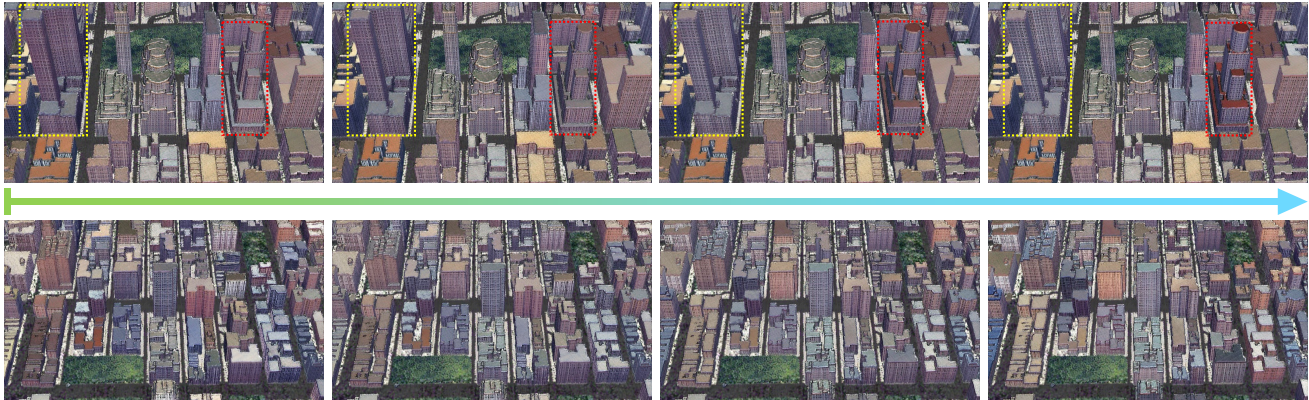


Figure 9. **Linear interpolation along the building style.** The style of each building gradually changes from left to right. In the first row, only the styles of the buildings enclosed by the bounding boxes are modified, while in the second row, the styles of all the buildings are changed.

B.2. Relighting

From the explicit representation of 3D Gaussians, relighting is much simpler than NeRF-based methods. Using Luma AI’s 3D Gaussians Plugin ¹, the generated city can be imported into Unreal Engine, enabling highly realistic lighting effects, as illustrated in Figure 10. However, the plugin is still under development, so shadow effects are not well generated. We believe this issue will be resolved soon.



Figure 10. **Relighting effects in Unreal Engine 5.** From left to right, the relighting effect is shown with increasing light intensity.

¹<https://www.unrealengine.com/marketplace/product/66dd775fa3104ecfb3ae800b8963c8b9>

B.3. Additional Qualitative Comparison

In Figures 11, 12 and 13, we provide more visual comparisons with state-of-the-art methods on GoogleEarth and KITTI-360, respectively.

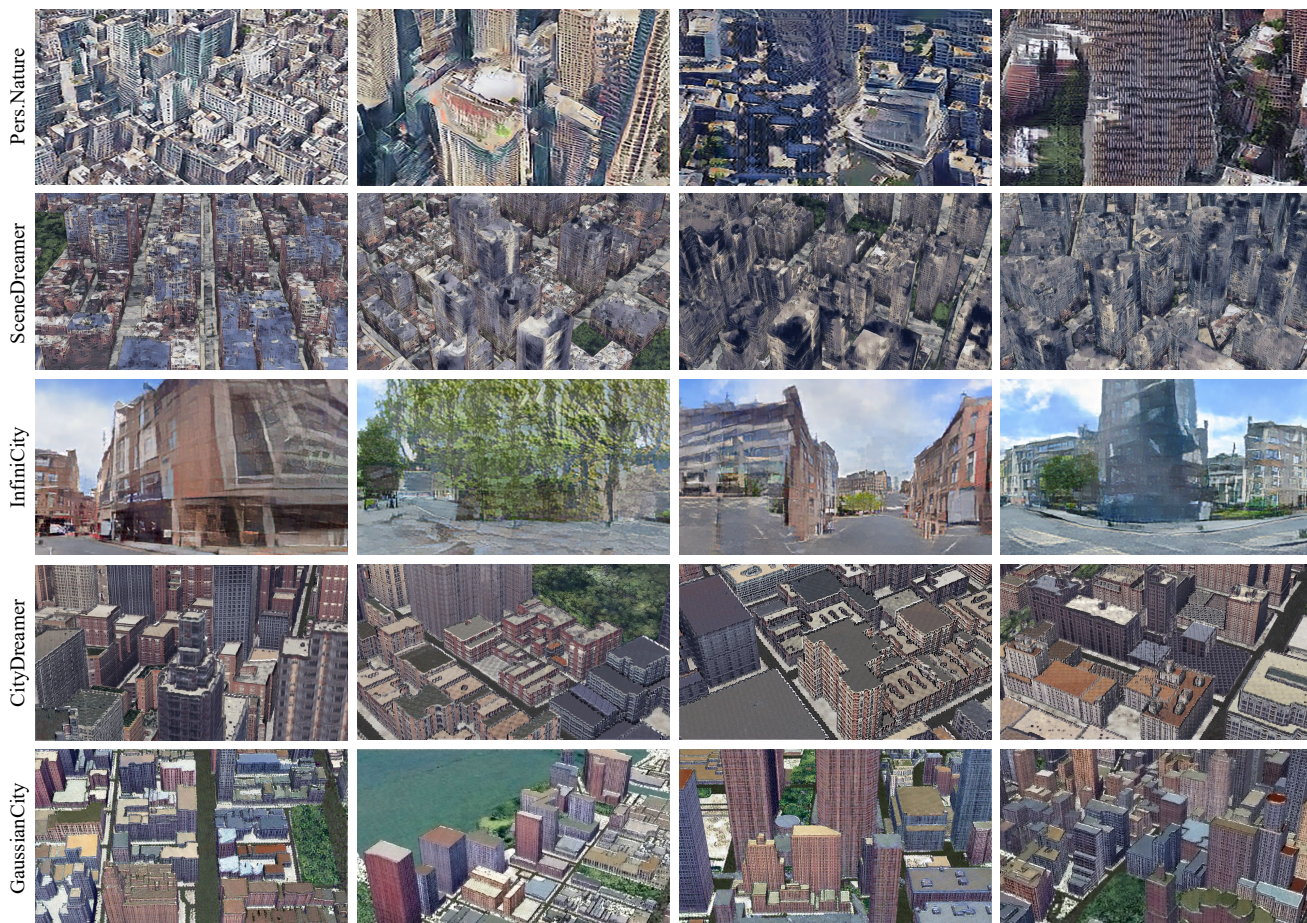


Figure 11. **Qualitative comparison on GoogleEarth.** Note that “Pers.Nature” is short for “PersistentNature” [7]. The visual results of InfiniCity [30] are provided by the authors and zoomed for optimal viewing.

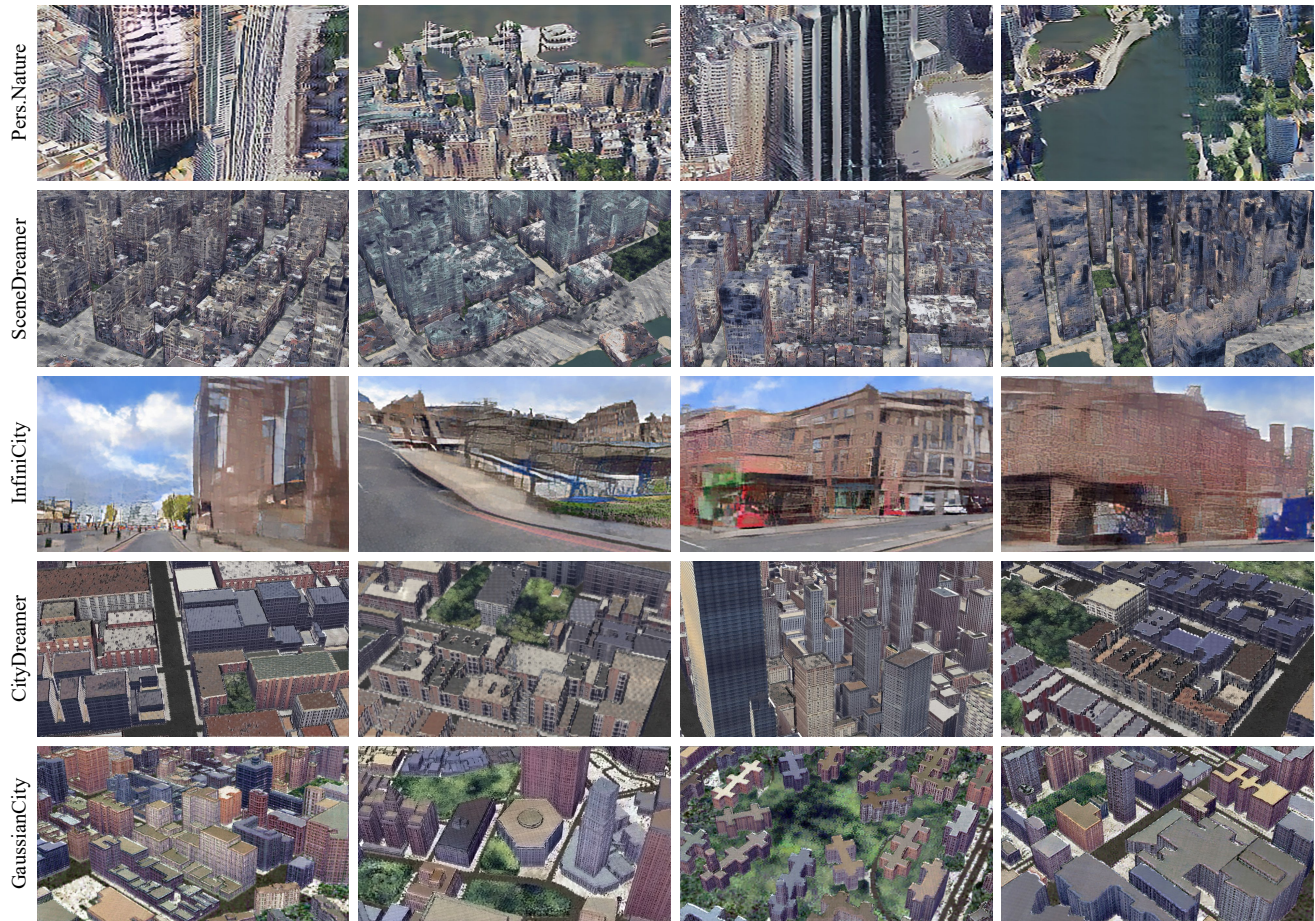


Figure 12. **Qualitative comparison on GoogleEarth.** Note that “Pers.Nature” is short for “PersistentNature” [7]. The visual results of InfiniCity [30] are provided by the authors and zoomed for optimal viewing.



Figure 13. **Qualitative comparison on KITTI-360.** The visual results of UrbanGIRAFFE [58] are provided by the authors since the training code and pretrained model are unavailable.